Available online at www.sciencedirect.com
ScienceDirect
International Journal of Heat and Mass Transfer 50 (2007) 3035–3046
International Journal of HEAT and MASS TRANSFER
www.elsevier.com/locate/ijhmt

Stabilities of combined radiation and Rayleigh–Bénard–Marangoni convection in an open vertical cylinder

B. Xu *, X. Ai, B.Q. Li

School of Mechanical and Materials Engineering, Washington State University, Pullman, WA 99164, USA

Received 4 April 2006; received in revised form 22 November 2006
Available online 23 March 2007

Abstract

This paper studies the combined radiation and natural convection in an open vertical cylinder. The cylinder is heated through its sidewall at a constant heat flux and cooled at the top surface via radiation. The high order finite difference method is used to simulate the fluid flow and heat transfer inside the cylinder and the internal radiation is solved using discontinuous finite element method. The two numerical methods are coupled through an iterative process. Based on the numerical simulations, a linear stability analysis is carried out to investigate how the internal radiation changes the stability of the flow.

Keywords: Marangoni flow; Linear stability analysis; Internal radiation; Discontinuous finite element method; High order finite difference method

1. Introduction

It is well known that convective flow in materials processing systems causes major macroscopic defects in the crystal produced [1]. In the efforts of developing of convection control mechanism that can be used to develop better quality crystals, it is crucial to understand the physics underlying the convection and the stability of the flow. There are extensive previous works on this topic. In most of the previous investigations on convective heat transfer, it is a common practice that the contribution of thermal radiation is neglected. However, there are many engineering applications in which the radiation can significantly interacts with the convection and change the heat transfer mechanism [2,3]. In materials processing systems, the fact that the melt is absorbing, emitting and scattering in thermal radiation frequency range makes it important to understand the interaction between the convective heat transfer and the thermal radiation [4–6]. The changes in thermal field caused by the radiation may change the convective flow field and furthermore, change the crystal structure of the materials produced.

Several previous works are found on the problem of combined radiation and convection [7–10]. A review on this problem is given by Yang [11]. More recently, Tan and Howell [12] presented a numerical study on combined thermal radiation and convection in a square enclosure. The radiative transport equation is discretized using product-integral method while the equations of momentum and energy conservations are discretized using finite difference method. It was found that the presence of internal radiation changes the temperature and flow fields significantly. Kassemi and Naraghi [13] investigated the combined radiation and convection in a square box in both terrestrial and microgravity environment using discrete exchange factor method. Their results have shown that the radiation significantly changes the flow and temperature fields in both terrestrial and microgravity applications. In microgravity environment, convection is weak and radiation can easily become the dominant heat transfer mode. The effect of internal radiation on oxide melts was discussed by Tsukada et al., [14]. The P-1 method was used to approximate the radiative heat transfer. The solid-liquid interface shape

* Corresponding author. Current address: EXA Corporation, 17177 N. Laurel Drive, Suite 441, Livonia, MI 48152, USA. Tel.: +1 734 432 0291; fax: +1 734 432 0054.
E-mail address: bing@exa.com (B. Xu).

0017-9310/$ - see front matter © 2007 Elsevier Ltd. All rights reserved.
doi:10.1016/j.ijheatmasstransfer.2007.01.007

Nomenclature

A	aspect ratio
$\mathbf{f}$	body force
Gr	Grashof number
$\mathbf{F}$	force matrix
g	gravity acceleration
H	height of crucible
h	heat transfer coefficient
I	radiative intensity
$\mathbf{K}$	stiffness matrix
k	thermal conductivity
M	Mach number
Ma	Marangoni number
m	Azimuthal wave number
$\mathbf{n}$	out normal of boundary
Pr	Prandtl number
P	kinematic pressure
p	dimensionless pressure
q	heat flux
R	cylinder radius
$\mathbf{r}$	position vector
Ra	Rayleigh number
Rad	radiation number
Re_γ	Marangoni Reynolds number
$\mathbf{s}$	direction vector
T	temperature
T_{amb}	ambient temperature
T_0	reference temperature
t	time
U	velocity component
$\mathbf{u}$	velocity vector

Greek symbols

α	thermal diffusivity
β	thermal expansion coefficient extinction coefficient
γ	negative rate of change of surface tension with temperature
ε	emissivity
θ	azimuthal angle
σ	surface tension scattering coefficient
σ_s	Stefan–Boltzmann constant
ϕ	shape function
φ	polar angle
κ	absorption coefficient
μ	viscosity
ν	kinematic viscosity
ρ	density
Ω	radiation control angle
ω	complex wave speed

Subscripts

amb	ambient
0	reference state
w	wall
z	z direction
θ	θ direction

becomes more convex to the melt as the optical absorption coefficients of both the crystal and the melt decreases. A numerical model for transport and solidification phenomena in oxide melts with and without the presence of an applied magnetic field was proposed by Shu et al. [6]. The model is base finite element solution of Navier–Stokes equations with the induced Lorentz force serving as the damping source. The radiative transfer equation was solved by discontinuous finite-element method. The stability of the combined convection and radiation was studied by Arpaci and Gözüm [15] and Arpaci and Bayazitoğlu [16], who found that the internal radiation stabilized the natural convection. Most recently, researches on the combined radiation and convection are be found by Lienhard V [17] and Bdéoui and Soufiani [18].

In this paper, the Rayleigh–Bénard–Marangoni convection in a vertical cylinder is investigated numerically. The cylinder is heated through its sidewall and cooled at the top free surface. The fluid flow and heat transfer equations are solved using high order finite difference method and a discontinuous finite element model is developed to solve the radiative transfer equation. The internal radiation is coupled into the convection through radiative heat source via an iterative process. Numerical simulations are carried out at various radiative parameters and significant changes in temperature profiles are observed due to the internal radiation. A linear stability analysis is carried out base on the numerical simulation to investigate how the internal radiation may change the stability diagrams of the melt flow at various radiative boundary conditions. The mechanism of the instability is also discussed.

2. Problem statements

The crucible under investigation, which is essentially a vertical cylinder with open top surface, is shown in Fig. 1. The cylinder has a height of H and a radius of R. A constant heat flux is supplied at the vertical wall and the bottom is adiabatic. At the top surface, the radiative heat exchange with the ambient is assumed. The cylindrical coordinate system used in the present study is also shown in Fig. 1.

2.1. Governing equations

The melts inside the crucible is considered incompressible fluid to which Boussinesq approximation applies. The surface tension is only a function of temperature,

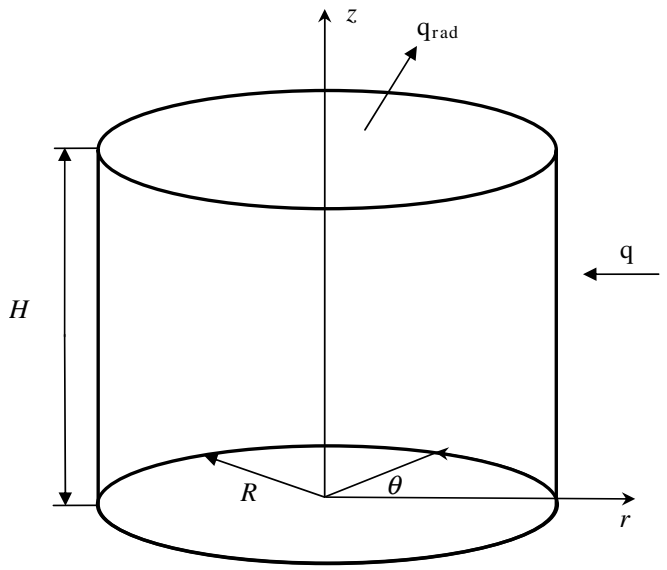

Fig. 1. Schematics of the vertical cylinder under investigation.

$$\sigma = \sigma_0 - \gamma(T - T_0), \tag{1}$$

where σ is the surface tension, T the fluid temperature, $\gamma = -\mathrm{d}\sigma/\mathrm{d}T$ the negative rate of change of surface tension with temperature and subscript 0 denotes a reference state. The melt flow is governed by the conservational laws of mass, momentum and energy, which are given as

$$\nabla \cdot \mathbf{u} = 0, \tag{2}$$

$$\frac{\partial \mathbf{u}}{\partial t} + (\mathbf{u} \cdot \nabla)\mathbf{u} = -\nabla p + \nabla^2 \mathbf{u} - Gr(T - T_0)\mathbf{g}, \tag{3}$$

$$\frac{\partial T}{\partial t} + (\mathbf{u} \cdot \nabla)T = \frac{1}{Pr}\nabla^2 T - \nabla \cdot \mathbf{q}(\mathbf{r}), \tag{4}$$

where $\mathbf{u}$ is the velocity vector, t the time, p the pressure, $\mathbf{g}$ the unit downward vector in z direction, T the temperature, T_0 the reference temperature and $\nabla \cdot \mathbf{q}(\mathbf{r})$ the radiative heat source. Gr is the Grashof number defined by $Gr = \frac{g\beta T_0 R}{\nu^2}$ and $Pr = \frac{\nu}{\alpha}$ the Prandtl number, where β is the thermal expansion coefficient, ν the kinetic viscosity, and α the thermal diffusivity. Eqs. (2)–(4) were obtained using following scale factors: R for length, ν/R for velocity, T_0 for temperature, R^2/ν for time, and $\rho\nu^2/R^2$ for pressure, where ρ is the density.

The governing equations (Eqs. (2)–(4)) are subject to the following boundary conditions. At the free surface ($z = H$ and $0 < r < R$),

$$\frac{\partial u_r}{\partial z} = Re_\gamma \frac{\partial T}{\partial r}, \tag{5}$$

$$\frac{\partial u_\theta}{\partial z} = Re_\gamma \frac{\partial T}{r\partial \theta}, \tag{6}$$

$$u_z = 0, \tag{7}$$

$$\frac{\partial T}{\partial z} = -\mathrm{Rad}\left(T^4 - T_{\mathrm{amb}}^4\right), \tag{8}$$

where $Re_\gamma = \frac{\gamma T_0 R}{\mu\nu}$ is the Marangoni–Reynolds number, $\mathrm{Rad} = \frac{\sigma_s \varepsilon T_0^3 R}{k}$ the radiation number, T_{amb} the temperature of ambient air, μ the dynamic viscosity, σ_s the Stefan–Boltzmann constant, ε the emissivity, and k the thermal conductivity. Considering the temperature range at which the material processing systems work, only radiative heat loss is considered at the free surface. At the vertical wall ($0 \leqslant z \leqslant H, r = R$),

$$u_r = u_z = u_\theta = 0, \tag{9}$$

$$\frac{\partial T}{\partial r} = \mathbf{q} \cdot \mathbf{n}_r, \tag{10}$$

where $\mathbf{q}$ is the heat flux at the vertical wall and $\mathbf{n}_r$ the unit vector in r direction. At the bottom ($z = 0, 0 \leqslant r \leqslant R$)

$$u_r = u_z = u_\theta = \frac{\partial T}{\partial z} = 0. \tag{11}$$

When temperature gradient along the free surface is low enough, flow in the crucible is axisymmetric, therefore at the centerline ($0 \leqslant z \leqslant H, r = 0$),

$$u_r = u_\theta = 0. \tag{12}$$

$$\frac{\partial u_z}{\partial r} = \frac{\partial T}{\partial r} = 0. \tag{13}$$

Note that in Eqs. (5) and (6), the surface tension gradient induced by temperature gradient along the free surface is balanced by shear stress. Eq. (7) assures that the free surface is flat and non-deformable.

2.2. Radiative transfer equation

The radiative heat transfer in the melt is described by the following integral-differential equation [2,3]:

$$\frac{\partial I(\mathbf{r},\mathbf{s})}{\partial s} = -\beta(\mathbf{r})I(\mathbf{r},\mathbf{s}) + \kappa(\mathbf{r})I_b(\mathbf{r}) + \frac{\sigma(\mathbf{r})}{4\pi}\int_{4\pi} I(\mathbf{r},\mathbf{s}')\Phi(\mathbf{s},\mathbf{s}')\,\mathrm{d}\Omega' \tag{14}$$

where $I(\mathbf{r},\mathbf{s})$ is the radiation intensity, $\beta(\mathbf{r}) = \kappa(\mathbf{r}) + \sigma(\mathbf{r})$ the extinction coefficient, $\kappa(\mathbf{r})$ the absorption coefficient, $\sigma(\mathbf{r})$ the scattering coefficient and Ω the solid angler,

To solve the radiative transfer equation given in Eq. (14), the following radiative boundary conditions are applied to the cylinder. At the vertical wall, bottom and top surface, diffusive grey surfaces are assumed as,

$$I(\mathbf{r},\mathbf{s}) = \varepsilon(\mathbf{r})I_b(\mathbf{r}) + \frac{1-\varepsilon(\mathbf{r})}{\pi}\int_{\mathbf{s}'\cdot\mathbf{n}_w<0} I(\mathbf{r},\mathbf{s}')|\mathbf{s}'\cdot\mathbf{n}_w|\,\mathrm{d}\Omega', \tag{15}$$

where ε is the boundary emissivity, $\mathbf{n}_w$ the normal direction of the boundary. Along the center line $r = 0$, symmetric boundary condition is used for the radiative transfer equation as

$$\begin{cases} I(\mathbf{r},\mathbf{s}) = I(\mathbf{r},\mathbf{s}^*) \\ \mathbf{n}\cdot\mathbf{s} = -\mathbf{n}\cdot\mathbf{s}^* \\ \mathbf{s}\times\mathbf{s}^*\cdot\mathbf{n} = 0 \end{cases} \tag{16}$$

where the $\mathbf{s}^*$ is the symmetric vector of radiation direction $\mathbf{s}$, in respect to the tangent of the boundary, with both $\mathbf{s}$ and $\mathbf{s}^*$ lying on the plane of $\mathbf{t}$–$\mathbf{n}$.

The internal radiation is coupled with other heat transfer modes through radiative heat source, which is calculated by

$$\nabla \cdot \mathbf{q}(\mathbf{r}) = \kappa\left(4\sigma_s T^4(\mathbf{r}) - \int_{4\pi} I(\mathbf{r},\mathbf{s})\,d\Omega\right), \tag{17}$$

where σ_s is the Stefan–Boltzmann constant and $\nabla \cdot \mathbf{q}(\mathbf{r})$ is the radiative heat source in Eq. (4) to couple the internal radiation with other modes of heat transfer. At the boundaries, the heat flux due to the internal radiation is calculated by

$$q_w(\mathbf{r}) = \varepsilon\left(\sigma_s T_w^4 - \int_{\mathbf{s}\cdot\mathbf{n}_w<0} I(\mathbf{r},\mathbf{s})\mathbf{s}\cdot\mathbf{n}_w\,d\Omega\right) \tag{18}$$

where T_w is the wall temperature. The boundary heat flux is positive when the flux is pointing outward. The boundary conditions presented in the last section are modified to balance the radiative heat flux given in Eq. (18).

2.3. Linear stability analysis

The governing equations and the boundary conditions presented above are solved numerically for axisymmetric base flow. Stability of the obtained velocity field $(\bar{U}_r, \bar{U}_z, 0)$, pressure $\bar{P}$ and temperature $\bar{T}$ are investigated by applying infinitesimal disturbance to the base flow

$$\begin{pmatrix} U_r \\ U_z \\ U_\theta \\ P \\ T \end{pmatrix} = \begin{pmatrix} \bar{U}_r \\ \bar{U}_z \\ 0 \\ \bar{P} \\ \bar{T} \end{pmatrix} + \begin{pmatrix} \hat{U}_r(r,z) \\ \hat{U}_z(r,z) \\ \hat{U}_\theta(r,z) \\ \hat{P}(r,z) \\ \hat{T}(r,z) \end{pmatrix} \exp(\mathrm{i}m\theta + \varpi t). \tag{19}$$

The last term of the right hand side of Eq. (19) is the small perturbation applied to the base flow where m is the azimuthal wave number, i the square root of -1 and ω the complex wave speed which is given by

$$\varpi = \varpi_r + i\varpi_i. \tag{20}$$

Here ω_i is the azimuthal frequency of oscillation, and ω_r determines the degree of amplification or damping. According to linear stability, when $\omega_i = 0$, the disturbance grow or decay monotonically. When $\omega_i \neq 0$, the perturbation is oscillatory with wave speed of ω_i. The perturbation are decays and the base flow is stable if $\omega_r < 0$. When $\omega_r > 0$ the perturbation grows with time and the base flow loses its axisymmetry. The neutral state is determined by $\omega_r = 0$.

To carry out the stability analysis, the governing equations are re-written with an assumption of slight compressibility as [19],

$$\frac{\partial p}{\partial t} + (\mathbf{u}\cdot\nabla)P + \frac{1}{M}\nabla\cdot\mathbf{u} = 0, \tag{21}$$

$$\frac{\partial \mathbf{u}}{\partial t} + (\mathbf{u}\cdot\nabla)\mathbf{u} = -\frac{1}{M}\nabla P + \left[\nabla^2\mathbf{u} + \frac{1}{3}\nabla(\nabla\cdot\mathbf{u})\right] + \mathbf{f}, \tag{22}$$

$$\frac{\partial T}{\partial t} + \mathbf{u}\cdot\nabla T = \frac{1}{Pr}\nabla^2 T - \nabla\cdot\mathbf{q}(\mathbf{r}). \tag{23}$$

Here, M denotes the Mach number in the fluid, P the kinematic pressure and $\mathbf{f}$ is the body force. Substituting Eqs. (19) and (20) into Eqs. (21)–(23) and subtracting the base flow from it, we obtain the final perturbation equations from which the complex wave speed ω can be determined. For the stability analysis, the basic state is solved using the governing equations with slight compressibility assumption. The slight compressibility is introduced there to overcome the singularity of the spectrum of generalized eigenvalue problem of incompressible flow [19].

3. Numerical schemes

Details on the numerical schemes used in the present study are given by Ai [20], hence only a brief description is presented here. The base flow is solved using high order finite difference method because of its spectral-like accuracy, computational efficiency and outstanding flexibility in dealing with irregular geometry and various boundary conditions. The spatial derivatives are discretized by the compact method. In the present model, the high order finite difference model is developed using compact central difference scheme, which has a fourth order accuracy in the approximations of both the first and the second order spatial derivatives. The fourth-order compact approximation derived by means of 5-point Legendre interpolation is adopted here. In the present numerical model, time integration is carried out by using the method of the combined Runge–Kutta and fractional step, as presented by Le and Moin [21]. The method is based on the predictor–corrector algorithm, which is one of the Runge–Kutta methods. In this method, each time step is divided into three sub-steps. At each sub-step, the KM time-splitting scheme developed by Kim and Moin [22] is used along with the staggered mesh to handling the pressure term.

The discontinuous finite element method is applied to solve the radiative transfer equation. Same as of its continuous counterpart, the first step of the discontinuous finite element formulation is to discretize the computational domain into a collection of finite elements. It is worth noting that using the discontinuous finite element, the solid angles are discretized in the framework of finite element space so that the conservation laws are observed, while most of the other numerical methods the solid angle integration is carried out using discrete ordinates. At the inner element boundaries, the inflow jump conditions applied

$$[I]_j = \begin{cases} [I]_j & \text{if } \mathbf{n}\cdot\mathbf{s} < 0 \\ 0 & \text{if } \mathbf{n}\cdot\mathbf{s} > 0 \end{cases}, \tag{24}$$

where $[I]_j = I_j^+ - I_j^-$ is the jump across the element boundaries.

Following the standard procedure for discontinuous finite element formulation, Eq. (14) can be solved. Assembling all these discretized terms together for each element, the final discretized equation can be expressed in terms of the following matrix form:

$$\mathbf{KU} = \mathbf{F}, \tag{25}$$

where $\mathbf{U}$ contains the unknown intensity vector and the matrix elements are summarized as follows:

$$K_{ij} = \int_{V_e} \phi_i \nabla \phi_j \cdot \int_{\Delta\Omega_l} \mathbf{s} \, \mathrm{d}\Omega \mathrm{d}V + \int_{V_e} \phi_i \phi_j \beta \mathrm{d}V \int_{\Delta\Omega_l} \mathrm{d}\Omega + \sum_{k=1}^{Nd} \max\left(0, -\int_{\Delta\Omega_l} \mathbf{s}\cdot\mathbf{n}_k \, \mathrm{d}\Omega\right) \int_{\Gamma_k} \phi_i \phi_j \, \mathrm{d}\Gamma, \tag{26}$$

$$F_i = \int_{V_e}^{\phi_i} S(\mathbf{r},\mathbf{s}) \mathrm{d}V \int_{\Delta\Omega_l} \mathrm{d}\Omega + \sum_{k=1}^{Nd} \max\left(0, -\int_{\Delta\Omega_l} \mathbf{s}\cdot\mathbf{n}_k \, \mathrm{d}\Omega\right) \int_{\Gamma_k} \phi_i \phi_j I_{NB,j} \, \mathrm{d}\Gamma, \tag{27}$$

where Nd is the number of boundaries associated with the ith element. Full details of the discontinuous finite element solution of the radiative transfer equation are given by Cui and Li [23].

The combined heat convection and radiation calculations require iterative procedures. In the present study, the temperature distribution is calculated using the higher order finite difference method while the internal radiation intensities are calculated by the discontinuous finite elements. The iteration starts with the calculation of temperature without radiative heat transfer. The radiative intensity distribution, and hence the divergence of the radiative heat fluxes, are then calculated using the calculated temperature field. The radiation heat flux divergence is then treated as a heating source and the temperature distribution is updated. This process repeats itself until a convergence on temperature and intensity is obtained.

Using the compact high order finite difference method the final perturbation equations along with the boundary conditions are discretized, and the final equation is written in the form of an eigenvalue matrix equation,

$$\mathbf{AX} = \omega \mathbf{BX}, \tag{28}$$

where $\mathbf{A}$ and $\mathbf{B}$ are coefficient matrices, $\mathbf{X} = \{\hat{u}_r, \hat{u}_z, \hat{u}_\theta, \hat{T}, \hat{p}\}^T$ is an assembling vector of the eigenfunction. This matrix equation is solved by linear fractional transformation with banded matrix structure taken into account using the LAPACK library. The obtained leading eigenvalue determines the stability of the axisymmetric base flow.

4. Results and discussion

The present numerical model is used to study the Rayleigh–Bénard convection in a vertical cylinder. Consider a horizontal layer of fluid confined by a vertical cylindrical wall. The top and bottom surfaces of the liquid layer are in contact with rigid walls that are kept at different temperatures of 0 and 1, respectively. The sidewall is adiabatic. All solid walls are no-slip. This problem has been studied extensively [24–26]. Its neutral curves have been well established. For a cylinder of $R = H = 1$, the critical Rayleigh number $\left(Ra = \frac{g\beta\Delta T H^3}{\mu\kappa}\right)$ at various azimuthal wave numbers from the present numerical model are compared with those from the Charlson and Sani [24,25] and Wanschura et al. [26]'s work in Table 1. The most dangerous mode is found to be $m = 2$ by all of the three models. The critical Rayleigh numbers obtained from the present model are with in ±2% of those of Wanschura et al. [26] and ±10% of those of Charlson and Sani [24,25]. The critical Ra at various aspect ratios $\left(A = \frac{R}{H}\right)$ for $m = 1$ and 2 are plotted in Fig. 2. The critical Ra decreases as the aspect ratio of the cylinder is increased because the lager aspect ratio decreases the stabilizing effect of the sidewall. As the aspect ratio increases, the critical Ra for both azimuthal wave numbers approach the critical Rayleigh number for an infinite liquid layer, which is 1708 [27].

When the top surface is open to the ambient and the effect of the buoyancy is ignored ($Ra = 0$), convection may be driven by the Marangoni effect. For this case, the Critical Marangoni numbers $\left(Ma = \frac{\gamma\Delta T H}{\mu\kappa}\right)$ obtained using the present model are compared with those from Dauby et al. for a cylinder of aspect ratio of 1 in Table 2. As shown in the table, the present model is in good agreement with

Table 1
Comparison of critical Rayleigh numbers at various azimuthal wave numbers between our results and those of Charlson and Sani [22,23] and Wanschura et al. [24]

m	The present model	Charlson and Sani [22,23]	Wanschura et al. [24]
1	2914	3164	2875
2	2514	2687	2500
3	3342		
4	4952		

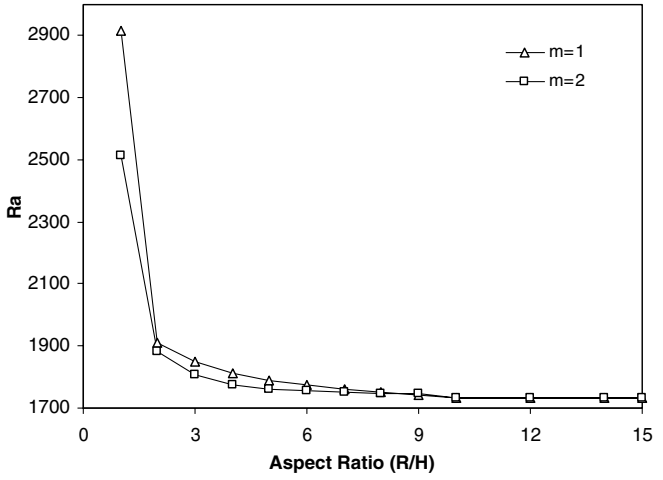

Fig. 2. Critical Rayleigh numbers for Rayleigh–Bénard convection in a vertical cylinder for $m = 1$ and $m = 2$ at various aspect ratios.

Table 2
Comparison of critical Marangoni numbers at various azimuthal wave numbers between our results and those of Dauby et al. [26]

m	This model	Dauby et al. [26]
0	169	163.57
1	122	109.08
2	162	160.15
3	261	257.86

Dauby et al's [28] results. The critical Ma for $m = 1$ and $m = 2$ at various aspect ratios are shown in Fig. 3. As the aspect ratio is increased, the sidewall effects decrease and therefore, the critical Marangoni number decreases and approaches the theoretic prediction of that for an unbounded layer of fluid, which is 79.6 [29]. The present model gives the critical Ma of 80 for both wave numbers when $A = 15$.

4.1. Convective flow of radiation participating melt in the vertical cylinder

A mesh dependency test is carried out to determine the mesh to be used in the present study. For the axisymmetric base flow, simulations were carried out for a cylinder of $R = H = 1$ with $Re_\gamma = 10^4, Gr = 6 \times 10^5, \kappa = 1\ \mathrm{m}^{-1}, \varepsilon = 1$ and $\sigma = 0\ \mathrm{m}^{-1}$. The velocities at $r = z = 0.6$ calculated using various uniform meshes are listed in Table 3. For a tradeoff between accuracy and computational load, a uniform grid with 26 nodes in both r and z directions ($N_r = N_z = 26$) is chosen to be used in simulation. Any further refinement will result in less than 2% error in base flow simulation. At each node, the solid angle is discretized into 8 elements in both the θ and φ directions. The other parameters used in the simulations are listed in Table 4. The tolerance for convergence is set to 10^{-5}. The results are plotted in dimensionless variable except for the temperature profiles, which are presented in primitive values.

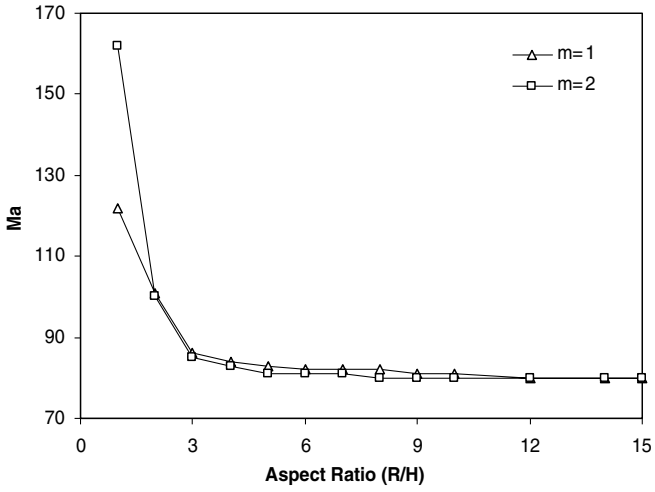

Fig. 3. Critical Marangoni numbers for Marangoni convection in a vertical cylinder for $m = 1$ and $m = 2$ at various aspect ratios.

Table 3
Velocity at $r = z = 0.6$ calculated using different uniform meshes for a crucible of $R = H = 1$ with $Gr = 6 \times 10^5, Re_\gamma = 10^4, \kappa = 1\ \mathrm{m}^{-1}, \varepsilon = 1$ and $\sigma = 0\ \mathrm{m}^{-1}$

N_r	N_z	Velocity
16	16	373.6055
21	21	398.6386
26	26	407.9187
31	31	414.7241
36	36	419.1348

Table 4
Parameters used in calculation

Parameter	Value
Aspect ratio (R/H)	1.0 (0.05 m/0.05 m)
Pr	0.02
Re_γ	10^4
q	1.0
Rad	1.0
T_{amb}	0.0
T_0	1000.0 K
M	10^{-6}

The flow and temperature fields for the convective flow for non-participating fluid in the cylinder with $Gr = 10^5$ are shown in Fig. 4. The fluid ascends near the solid wall and descends at the crucible center due to the Rayleigh–Bénard–Marangoni effect. The fluid temperature is higher near the vertical wall due to the constant heat flux supplied. When there is internal radiation, the velocity vectors and isothermals are plotted in Fig. 5 for $Gr = 10^5, \kappa = 1\ \mathrm{m}^{-1}, \varepsilon = 1$ and $\sigma = 0\ \mathrm{m}^{-1}$. In this case, the melt is absorbing, emitting but not scattering. Comparing Figs. 4b and 5b, the internal radiation has a strong effect on the temperature distribution. The temperatures near the vertical wall and the free surface are decreased. This is because that the presence of radiative heat flux at the boundaries requires higher temperature gradients to conduct the heat from the walls to ensure energy balance. Considering the reference temperature used in this case (1000 K), a strong heat flux is imposed at the boundaries, which decreases the melt temperature significantly. At the bottom, the isothermals are not orthogonal to the boundary due to the radiative heat flux at the bottom. For low Prandtl fluid flow, thermal field is only loosely coupled with velocity field. The internal radiation does not have a strong effect on the velocity profile.

The effects of the absorption coefficient are depicted in Fig. 6, which shows the velocity vectors and the temperature distribution for $\kappa = 5\ \mathrm{m}^{-1}, \varepsilon = 1$ and $\sigma = 0\ \mathrm{m}^{-1}$. A comparison between Figs. 5b and 6b indicates that the bulk temperature is raised by approximately 6 K due to the increase in absorption coefficient. A careful examination of the radiative transfer equation (Eq. (14)) reveals that when a medium is absorbing and emitting, but not scattering, the radiative intensity increases along a given direction **s**. Though the absorption and emission tend to increase the

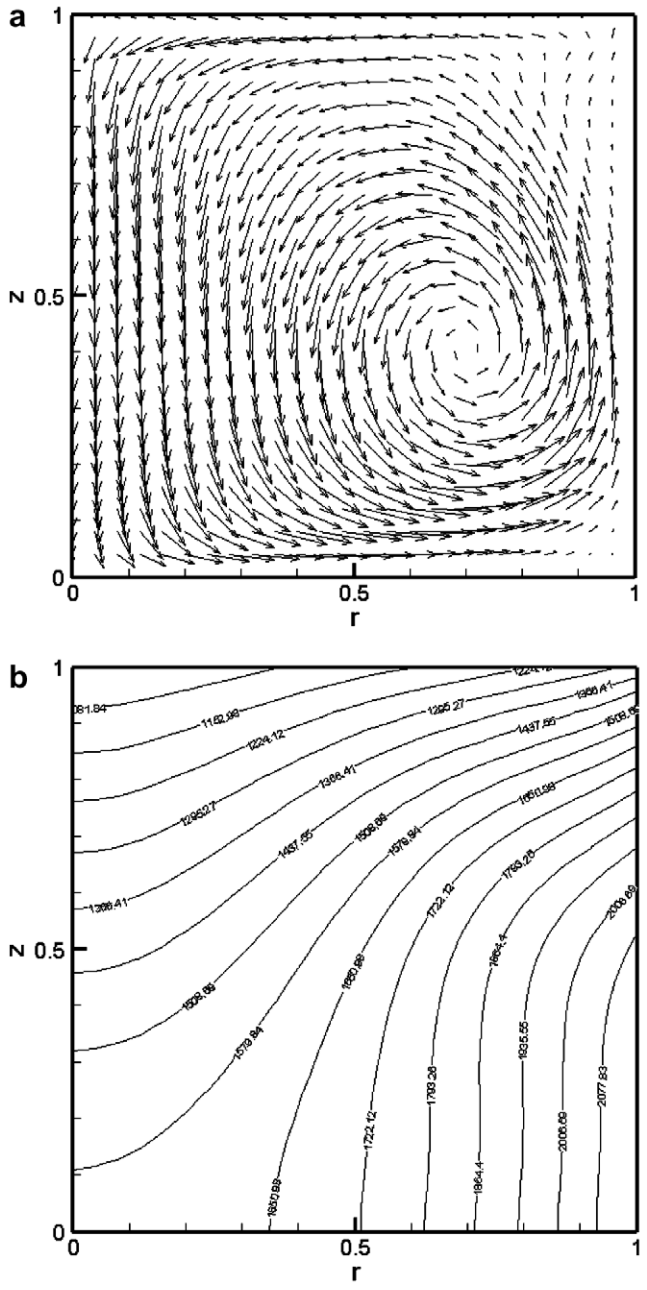

Fig. 4. Velocity field (a) and isotherms (b) of the convective flow corresponding to $Gr = 10^5$ and $\kappa = \varepsilon = \sigma = 0$.

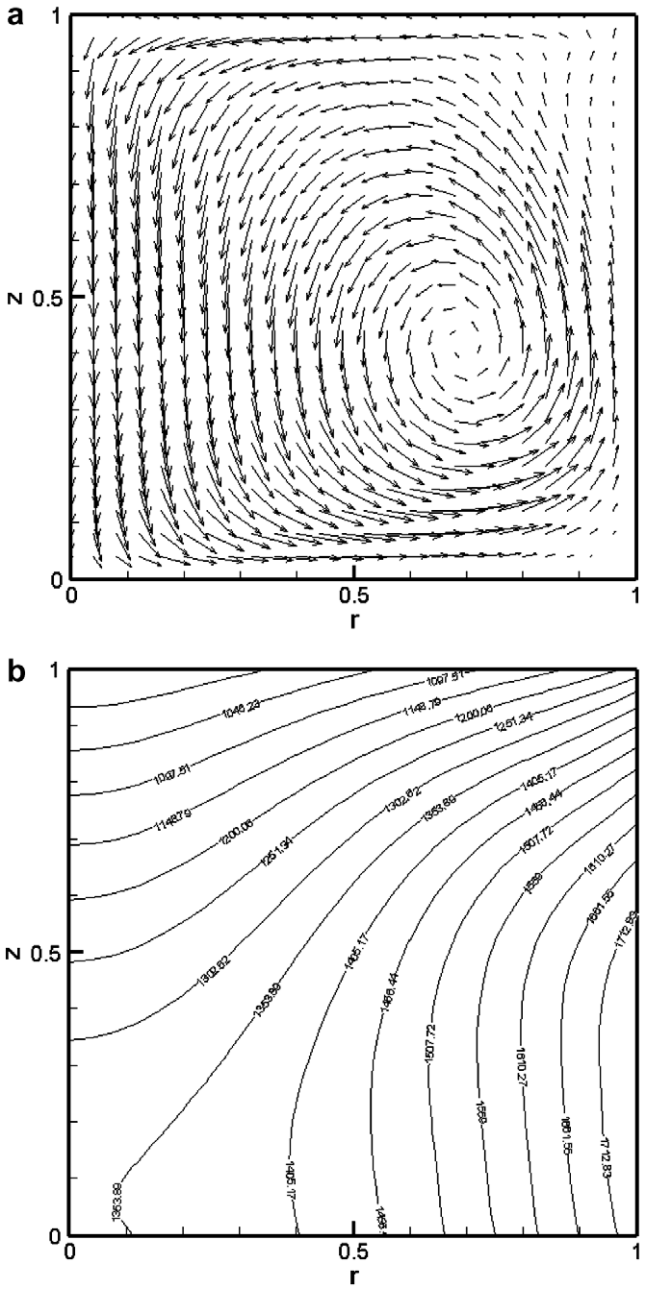

Fig. 5. Velocity field (a) and isotherms (b) of the convective flow corresponding to $Gr = 10^5, \kappa = 1\ \mathrm{m}^{-1}, \varepsilon = 1$ and $\sigma = 0\ \mathrm{m}^{-1}$.

melt temperature, the cooling effect from the boundary radiative heat flux is strong enough to suppress the heating effects and decrease the melt temperature.

To illustrate how the scattering changes the convective flow pattern, simulation was carried out at $Gr = 10^5, \kappa = 1\ \mathrm{m}^{-1}, \varepsilon = 1$ and $\sigma = 1\ \mathrm{m}^{-1}$, of which the velocity and temperature profiles are shown in Fig. 7. Only isotropic scattering is considered in the present study. Comparing with the non-scattering results shown in Fig. 5, it is observed that the melt temperatures near the boundaries are decreased due to the back scattering. The bulk melt temperature is decreased due to the scattering.

4.2. Stability of the convective flow

A linear stability analysis is carried out based on the numerical simulation results. The stability analysis is focused on how the radiative parameters affect the stability of the flow. The neutral curves are determined as functions of the azimuthal wave numbers and the critical Grashof numbers at which the real parts of the leading eigenvalues vanish.

Neutral curve for the convection of non-participating fluid in a cylinder of $R = H = 1, Re_\gamma = 10^4$ is shown in Fig. 8. Critical Grashof numbers are shown for azimuthal

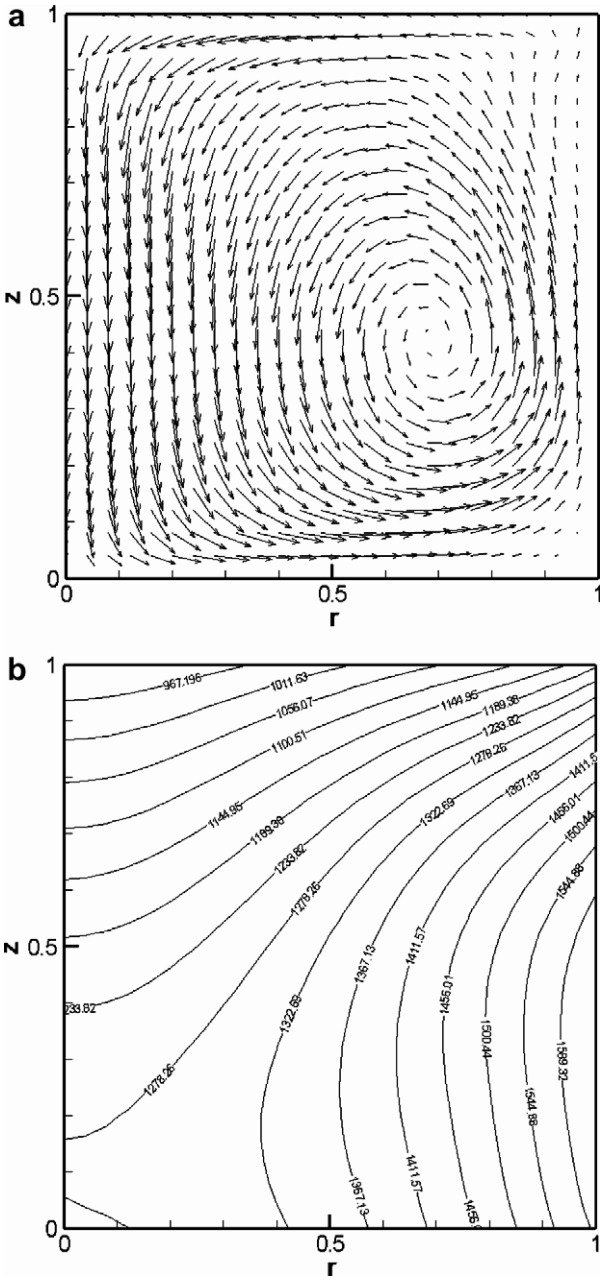

Fig. 6. Velocity field (a) and isotherms (b) of the convective flow corresponding to $Gr = 10^5, \kappa = 5\ \mathrm{m}^{-1}, \varepsilon = 1$ and $\sigma = 0\ \mathrm{m}^{-1}$.

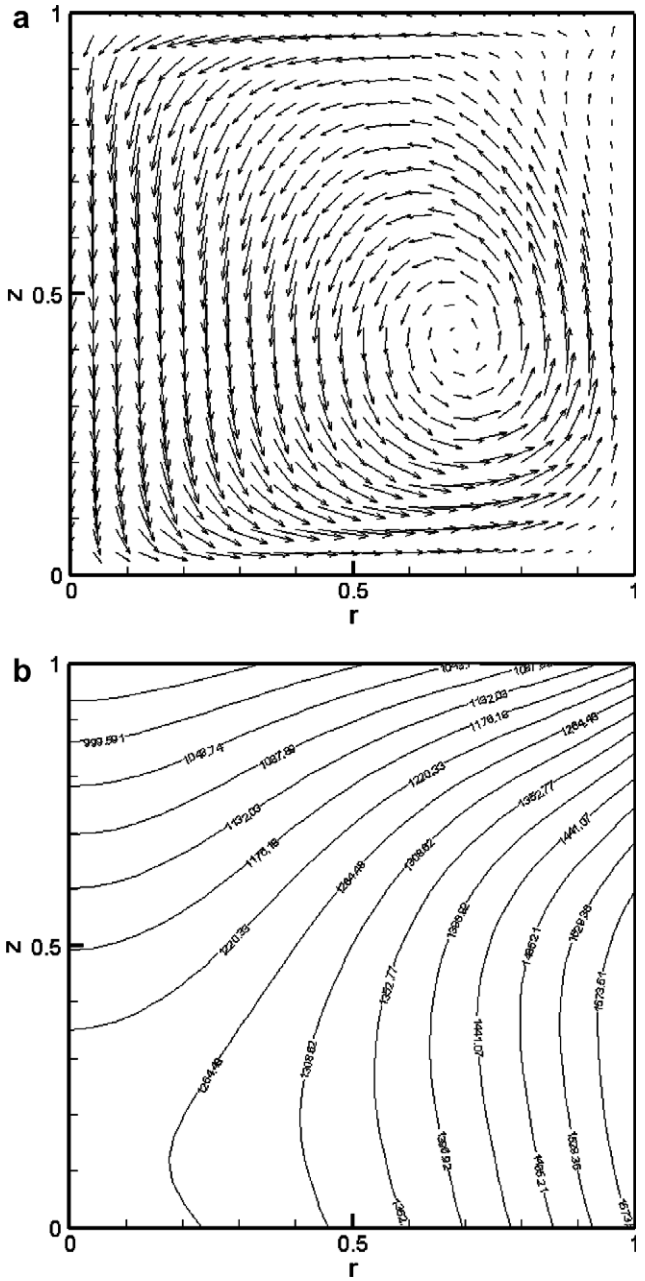

Fig. 7. Velocity field (a) and isotherms (b) of the convective flow corresponding to $Gr = 10^5, \kappa = 1\ \mathrm{m}^{-1}, \varepsilon = 1$ and $\sigma = 1\ \mathrm{m}^{-1}$.

wave numbers between 0 and 8 and the most dangerous mode is $m = 1$. Fig. 9 shows the critical Grashof numbers for absorbing, emitting but not scattering fluid in the same cylinder. The absorption coefficients, κ, used for the analysis are $1\ \mathrm{m}^{-1}$ and $5\ \mathrm{m}^{-1}$, respectively. The emissivity at the boundaries is 1. A comparison between Figs. 8 and 9 reveals that the presence of the internal radiation delays the onset of the instability. The critical Grashof number is increased from 281,224 for non-participating melt to 598,673 for $\kappa = 1\ \mathrm{m}^{-1}$ and 629,856 for $\kappa = 5\ \mathrm{m}^{-1}$. It is obvious that the internal radiation stabilized the convection and the stabilization effect increases as the absorption coefficient increases. The same stabilization effect has been observed in several previous works [15–18]. The most dangerous azimuthal mode is changed from 1 to 5 due to the internal radiation.

The stability diagrams at two different boundary emissivities, $\varepsilon = 0.5$ and 1, are depicted in Fig. 10. The neutral curves are obtained using the same crucible as the last case. The fluid has an absorption coefficient of $1.0\ \mathrm{m}^{-1}$. As it is expected, the critical Grashof numbers are increased due to the internal radiation. The critical Grashof number is 476,837 for $\varepsilon = 0.5$ and 598,673 for $\varepsilon = 1$. The most dangerous azimuthal mode is found to be 5.

Fig. 11 shows the neutral curves for an absorbing, emitting and scattering medium in the same crucible. The melt

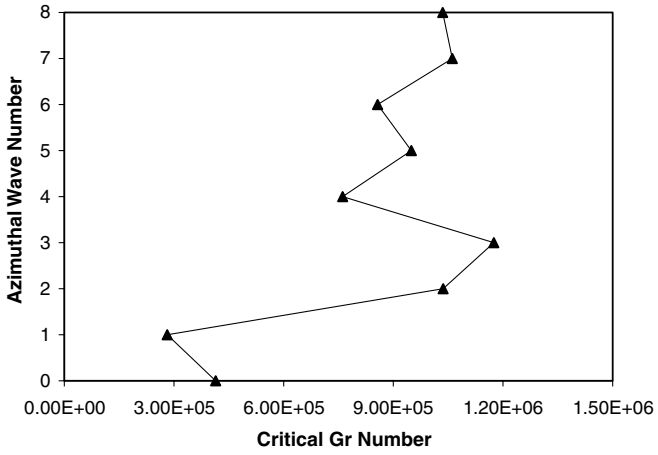

Fig. 8. Critical Grashof numbers for non-participating fluid of $\kappa = \varepsilon = \sigma = 0$.

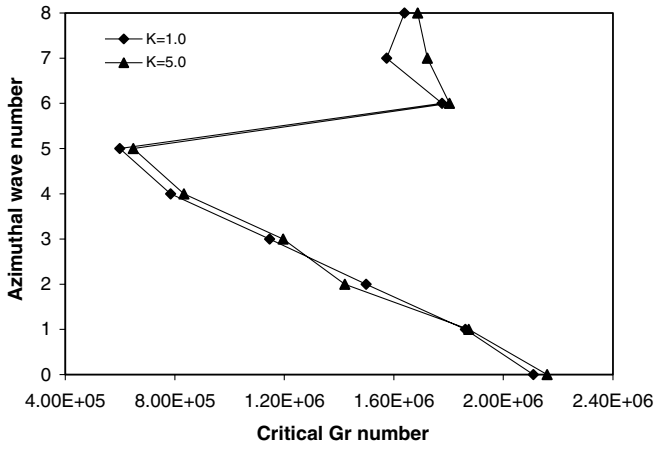

Fig. 9. Critical Grashof numbers at $\kappa = 1\ \mathrm{m}^{-1}$ and $5\ \mathrm{m}^{-1}$ for $\varepsilon = 1$ and $\sigma = 0$. The critical Grashof number for the corresponding radiative non-participating case is 281,224.

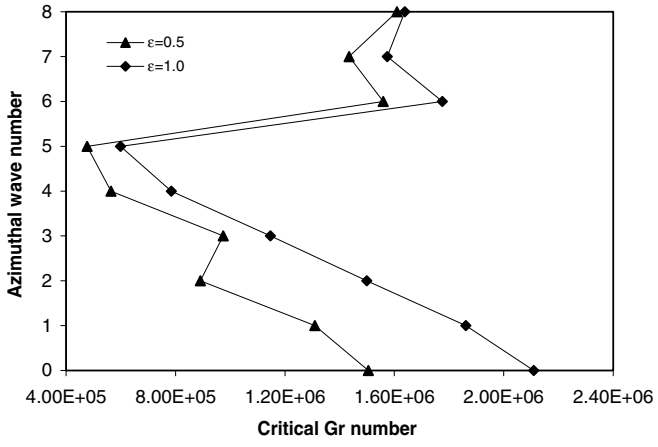

Fig. 10. Critical Grashof numbers at $\varepsilon = 0.5$ and 1 for $\kappa = 1\ \mathrm{m}^{-1}$ and $\sigma = 0$. The critical Grashof number for the corresponding radiative non-participating case is 281,224.

is absorbing at $\kappa = 1\ \mathrm{m}^{-1}$ and the stability curves are obtained at two different scattering coefficients of $0\ \mathrm{m}^{-1}$ and $1\ \mathrm{m}^{-1}$, respectively. With the presence of the scattering, the critical Grashof number is further increased, which is 641,827 when $\sigma = 1\ \mathrm{m}^{-1}$. Again, the most dangerous mode is found to be 5.

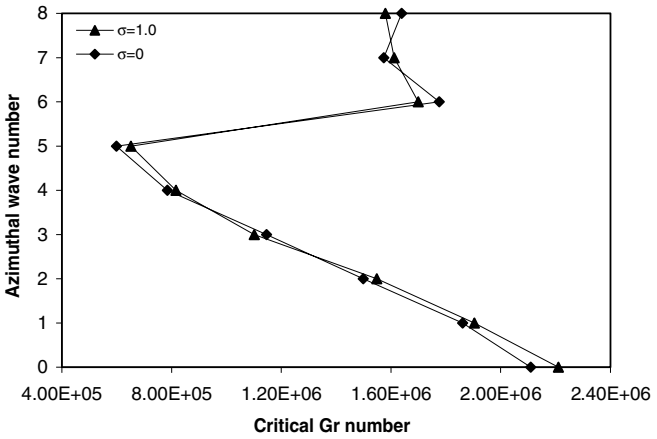

Fig. 11. Critical Grashof numbers at $\sigma = 0\ \mathrm{m}^{-1}$ and $1\ \mathrm{m}^{-1}$ for $\varepsilon = 1$ and $\kappa = 1\ \mathrm{m}^{-1}$. The critical Grashof number for the corresponding radiative non-participating case is 281,224.

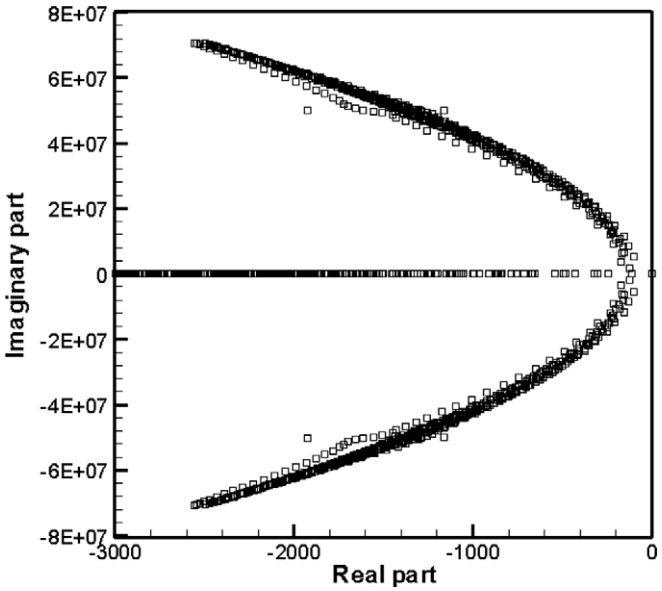

Fig. 12. Eigenvalue spectrum of critical base flow for $R = H = 1, Gr_{\mathrm{cr}} = 598,673$ at $\kappa = 1\ \mathrm{m}^{-1}, \varepsilon = 1$ and $\sigma = 0\ \mathrm{m}^{-1}$.

Table 5
First five leading eigenvalues for $R = H = 1, Gr_{\mathrm{cr}} = 598,673$ for $\kappa = 1\ \mathrm{m}^{-1}, \varepsilon = 1$ and $\sigma = 0\ \mathrm{m}^{-1}$

No.	ω_r	ω_i
1	-3.9947×10^{-5}	-1.31879×10^{-12}
2	−97.8257	±5325219.4564
3	−108.9957	±783.7622
4	−126.3728	±1841190.8140
5	−131.8824	±8505316.6937

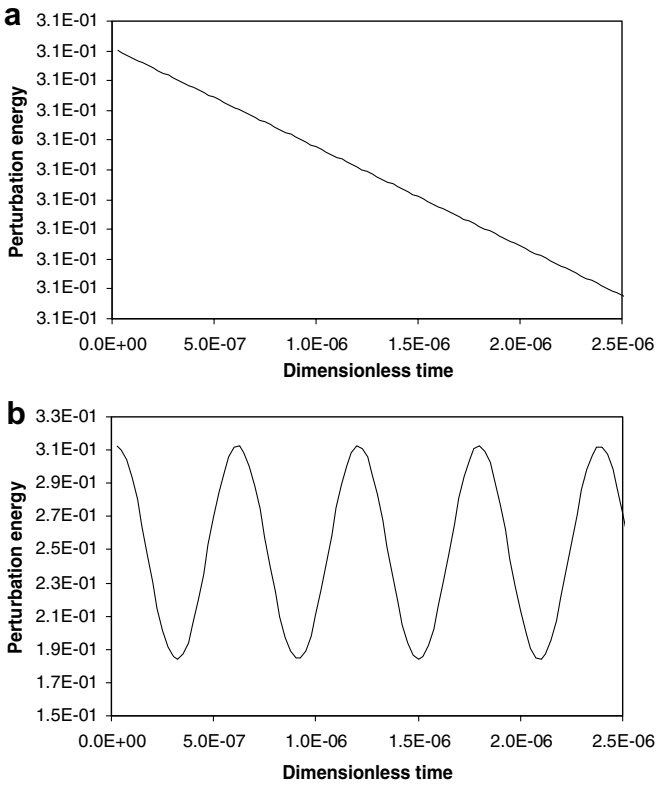

Fig. 13. Evolution of perturbation energy in the axisymmetric plane at $\theta = 0$ for $R = H = 1, Gr_{cr} = 598,673, Re_{\gamma} = 10^4, \kappa = 1\ \mathrm{m}^{-1}, \varepsilon = 1$ and $\sigma = 0\ \mathrm{m}^{-1}$: (a) first and (b) second leading eigenvalue.

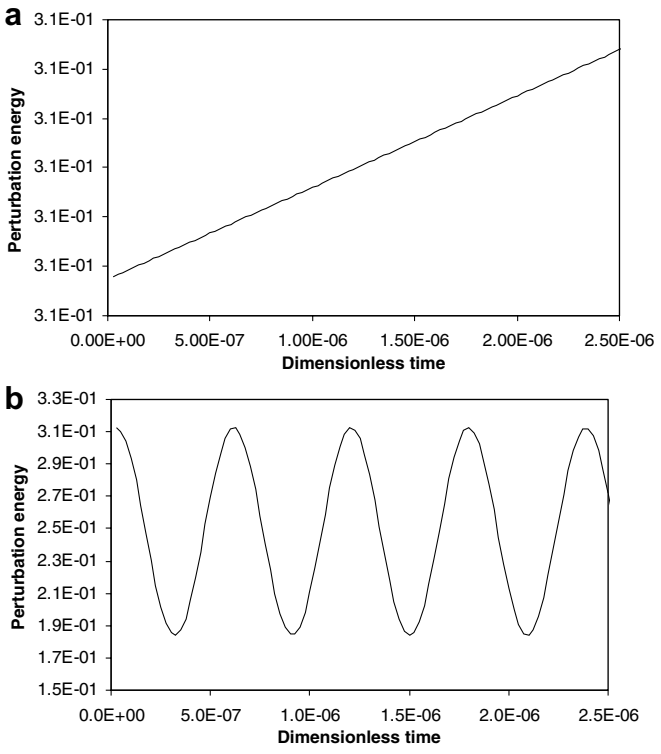

Fig. 14. Evolution of perturbation energy in the axisymmetric plane at $\theta = 0$ for $R = H = 1, Gr = 598,700, Re_{\gamma} = 10^4, \kappa = 1\ \mathrm{m}^{-1}, \varepsilon = 1$ and $\sigma = 0\ \mathrm{m}^{-1}$: (a) first and (b) second leading eigenvalue.

The typical eigenvalue spectrum at the critical state of $Gr_{cr} = 598,673$ for $\kappa = 1\ \mathrm{m}^{-1}, \varepsilon = 1$ and $\sigma = 0\ \mathrm{m}^{-1}$ is shown in Fig. 12. The eigenvalues could be either real numbers or conjugate complex pairs. The eigenvalue spectrum has T-shape structure. Table 5 lists the first five leading eigenvalues. The first leading eigenvalue is a real number while the rest four eigenvalues appear to be conjugate complex pairs, which implies that the first leading eigenvalue is in stationary mode while the following four eigenvalues are in Hopf mode. The transient evolution of the perturbation energy corresponding to the first two leading eigenvalues are plotted in Figs. 13 and 14 for $Gr = 598,673$ and 598,700, respectively. Fig. 13 shows the transient perturbation energy for the critical state at $Gr = 598,673$. The perturbation energy of the first leading eigenvalue decreases monotonically as time is increased (Fig. 13a). This monotonic profile confirms the T-shape eigenvalue spectrum shown in Fig. 12, in which the leading eigenvalue appears to be a real number ($\omega_i = 0$). The perturbation energy cor-

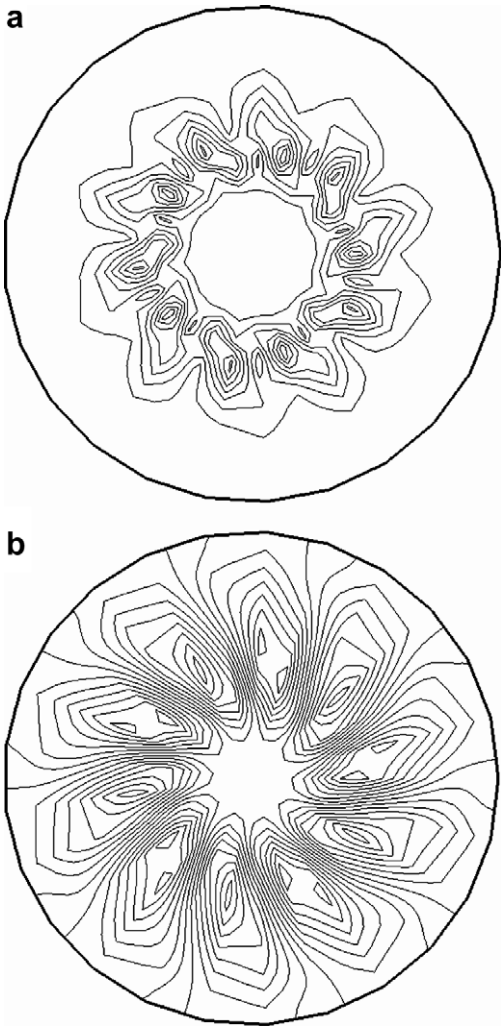

Fig. 15. Pattern of perturbation of for the leading eigenvalue at the $z = 0.5$ corresponding to $R = H = 1, Re_{\gamma} = 10^4, Gr_{cr} = 598,673, m = 5, \kappa = 1\ \mathrm{m}^{-1}, \varepsilon = 1$ and $\sigma = 0\ \mathrm{m}^{-1}$: (a) energy at $t = 2.5 \times 10^{-8}$; (b) temperature at $t = 2.5 \times 10^{-8}$.

responding to the second leading eigenvalue osculates at a frequency of ω_i, which is shown in Fig. 13b. Fig. 14 shows the temporal evolution the perturbation energy corresponding to the first two leading eigenvalues for an unstable base flow at $Gr = 598{,}700$. For this case, the perturbation energy of the leading eigenvalue increases monotonically, which confirms that the base flow is unstable. An oscillatory second leading eigenvalue perturbation energy profile similar to that for the critical case is observed in Fig. 13b.

The contours of the perturbation energy and temperature for the leading eigenvalue are shown in Fig. 15. As it is shown in the figure, because of the most dangerous mode of 5, the contours consist of five pairs of maxima and minima along the azimuthal direction. Fig. 16 shows the 3-D flow structure and free surface flow pattern constructed using the leading eigenvalue at the critical state of $R = H = 1, Re_\gamma = 10^4, Gr_{cr} = 598,673$ and $m = 5$ for $\kappa = 1\ \mathrm{m}^{-1}, \varepsilon = 1$ and $\sigma = 0\ \mathrm{m}^{-1}$. For this case, 10 co-rotating loops are observed along the azimuthal direction, which confirms the perturbation contours plotted in Fig. 15.

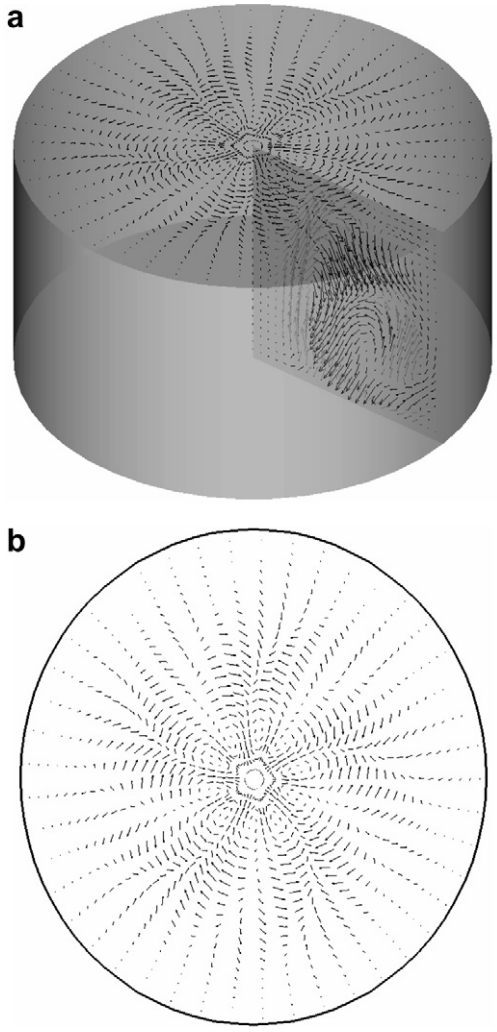

Fig. 16. Three-dimensional flow pattern of the leading eigenvalue corresponding to the critical state for $R = H = 1, Re_\gamma = 10^4, Gr_{cr} = 598673$ and $m = 5$: (a) 3-D flow structure; (b) top surface flow pattern.

5. Summary

In this paper, a numerical model was developed to simulate the Rayleigh–Bénard–Marangoni convection in a laterally heated vertical cylinder. Both radiation participating and non-participating fluids were considered. The discontinuous finite element was incorporated into the high order finite difference model presented in the last chapter via an iterative process.

The numerical has shown that the internal radiation has a significant effect on the convective flow pattern in the cylinder. The radiative heat flux imposed by the domain boundaries induced higher temperature gradient near the boundaries, which decreased the bulk temperature. In the mean time, the melt was heated by combined absorption, emission and scattering effects. However, the boundary heat flux was strong enough to suppress the internal radiation effect.

A linear stability analysis was carried out at various radiative boundary conditions based on the numerical simulation. It was found that the internal radiation stabilized the convective flow. The most dangerous mode changed from 1 to 5 due to the internal radiation. The instability mechanism is also discussed in this paper.

Acknowledgements

Partial support of this work by NASA (Grant No.: NAG8-NNM04AA17G) and DOE (Grant No.: DE-FC07-01ID14189) is gratefully acknowledged. This work was partially supported by the National Center for Supercomputing Applications under grant number CTS050035N and utilized the IBM P690.

References

[1] W.E. Langlois, Buoyancy-driven flows in crystal-growth melts, Annul. Rev. Fluid Mech. 17 (1985) 191–215.
[2] R. Siegel, J.R. Howell, Thermal radiation heat transfer, 3rd ed., Taylor & Francis, 1992.
[3] M.F. Modest, Radiative heat transfer, McGraw-Hill, Inc., New York, 1993.
[4] S. Brandon, J.J. Derby, Heat transfer in vertical Bridgman growth of oxides: effects of conduction, convection, and internal radiation, J. Cryst. Growth 121 (1992) 473.
[5] M. Kobayashi, T. Tsukada, M. Hozawa, Effect of internal radiative heat transfer on the convection in CZ oxide melt, J. Cryst. Growth 180 (1997) 157.
[6] Y. Shu, B.Q. Li, K.G. Lynn, Numerical modeling of internal radiation and solidification in semitransparent melts in magnetic field, Num. Heat Transfer, Part A 45 (2004) 957.
[7] D.W. Larson, Enclosed radiation and turbulent natural convection induced by a fire, in: R.W. Lewis, K. Morgan, O.C. Zienkiewicz (Eds.), Numerical Method in Heat transfer, Wiley, New York, 1984.
[8] L.C. Chang, K.T. Yang, J.R. Lloyd, Radiation-natural convection interaction in two-dimensional complex enclosures, ASME J. Heat Transfer 105 (1983) 89.

[9] G. Desreyaud, G. Lauriat, Natural convection of radiating fluid in a vertical layer, ASME J. Heat Transfer 107 (1985) 710.
[10] B.W. Webb, R. Viskanta, Radiation-induced buoyancy-driven flow in rectangular enclosures: experiments and analysis, ASME J. Heat Transfer 109 (1987) 427.
[11] K.T. Yang, Numerical modeling of natural convection-radiation interactions in enclosures, Heat Transfer 1986: Proc. Eighth Int. Heat Transfer Conf. 1, 131 Hemisphere, Washington, DC, (1987).
[12] Z. Tan, J.R. Howell, Combined radiation and natural convection in a two-dimensional participating square medium, Int. J. Heat Mass Transfer 34 (1991) 785.
[13] M. Kassemi, M.H.N. Naraghi, Analysis of radiation-natural convection interactions in 1-g and low-g environments using the discrete exchange factor method, Int. J. Heat Mass Transfer 36 (1993) 4141.
[14] T. Tsukada, K. Katsuyuki, M. Hozawa, Effect of internal radiation within crystal and melt on Czochralski crystal growth of oxide, Int. J. Heat Mass Transfer 38 (1995) 2707.
[15] V.S. Arpci, D. Gözüm, Thermal stability of radiating fluids: the Bénard problem, Phys. Fluids 16 (1973) 581.
[16] V.S. Arpci, Y. Bayazitoğlu, Thermal stability of radiating fluids: asymmetric slot problem, Phys. Fluids 16 (1973) 589.
[17] J.H. Lienard V, Thermal radiation in Rayleigh–Bénard instability, J. Heat Transfer 112 (1990) 100.
[18] F. Bdéoui, A. Soufiani, The onset of Rayleigh–Bénard instability in molecular radiating gases, Phys. Fluids 9 (1997) 3858.
[19] Y. Ding, Kawahara, Linear stability of incompressible fluid flow using a mixed finite element method, J. Comput. Phys. 139 (1998) 243.
[20] X. Ai, The instability analysis and direct numerical simulation of turbulent flows in electromagnetically levitated droplets, Ph.D. Thesis Washington State University, Pullman, WA, 2004.
[21] H. Le, P. Moin, An improvement of fractional step methods for the incompressible Navier–Stokes equations, Int. J. Numer. Meth. Fluids 2 (1991) 369.
[22] J. Kim, P. Moin, Application of a fractional-step method to incompressible Navier-Stokes equations, J. Comput. Phys. 59 (1985) 308.
[23] X. Cui, B.Q. Li, A discontinuous finite-element formulation for radiative transfer in axisymmetric finite cylindrical enclosures and coupling with mode heat transfer, Num. Heat Transfer, Part B 48 (2005) 317.
[24] G.S. Charlson, R.N. Sani, Thermoconvective instability in a bounded cylindrical fluid layer, Int. J. Heat Mass Transfer 13 (1970) 1479.
[25] G.S. Charlson, R.N. Sani, On Thermoconvective instability in a bounded cylindrical fluid layer, Int. J. Heat Mass Transfer 14 (1970) 2157.
[26] M. Wanschura, H.C. Kuhlmann, H.J. Rath Three-dimensional instability of axisymmetric buoyant convection in cylinder heated from below, J. Fluid Mech. 326 (1996) 339.
[27] R.G. Drazin, W.H. Reid, Hydrodynamic stability, The Cambridge University ‘ess, 1986.
[28] P.C. Dauby, G. Lebon, E. Bouhy, Linear Bénard–Marangoni instability in rigid circular containers, Phys. Rev. E 56 (1997) 520.
[29] J.R.A. Pearson, On convection cells induced by surface tension, J. Fluid Mech. 4 (1958) 489.